Complete sets of polarization transfer observables for the ^{208}Pb($\vec{p}, \vec{n}$) reaction at 296 MeV and Gamow-Teller and spin-dipole strengths for ^{208}Pb

T. Wakasa,[1,*] M. Okamoto,[1] M. Dozono,[2] K. Hatanaka,[3] M. Ichimura,[2] S. Kuroita,[1] Y. Maeda,[4] H. Miyasako,[4]
T. Noro,[1] T. Saito,[4] Y. Sakemi,[5] T. Yabe,[1] and K. Yako[6]

[1]*Department of Physics, Kyushu University, Higashi, Fukuoka 812-8581, Japan*
[2]*RIKEN Nishina Center for Accelerator-Based Science, The Institute of Physical and Chemical Research, Wako, Saitama 351-0198, Japan*
[3]*Research Center for Nuclear Physics, Osaka University, Ibaraki, Osaka 567-0047, Japan*
[4]*Department of Applied Physics, University of Miyazaki, Miyazaki, Miyazaki 889-2192, Japan*
[5]*Cyclotron and Radioisotope Center, Tohoku University, Sendai, Miyagi 980-8578, Japan*
[6]*Department of Physics, University of Tokyo, Bunkyo, Tokyo 113-0033, Japan*

We report measurements of cross sections and analyzing powers for reaction angles of $\theta_{\text{lab}} = 0.0°$–$10.0°$ and complete sets of polarization transfer observables and induced polarizations at $\theta_{\text{lab}} = 0.0°$–$7.0°$ for the ^{208}Pb($\vec{p}, \vec{n}$) reaction at a bombarding energy of $T_p = 296$ MeV. A multipole decomposition technique was applied to the data to extract the Gamow-Teller (GT) and spin-dipole (SD) components from the continuum. The polarization observables were also used, for the first time, to separate the SD components into different spin-parity transfer ($\Delta J^\pi = 0^-$, 1^-, and 2^-) contributions. A significant strength with $\Delta J^\pi = 1^+$ is identified in the continuum beyond the GT giant resonance, which is due to configuration mixing effects and the isovector spin monopole (IVSM) contribution. The SD strength distributions were clearly dependent on ΔJ^π, which is reasonably reproduced by Hartree-Fock (HF) plus random phase approximation (RPA) calculations that include the Skyrme interaction with tensor components [Phys. Rev. C **83**, 054316 (2011)].

I. INTRODUCTION

Spin-isospin excitations provide a unique opportunity to study the spin correlations in nuclei [1]. At small momentum transfers, the spin-isospin particle-hole interaction is strongly repulsive, and the residual interaction leads to collective excitations such as the Gamow-Teller (GT) and spin-dipole (SD) resonances. The quenching of the total GT strength [2] from the GT sum rule [3] (also called Ikeda's sum rule [4]) for $3(N - Z)$ has prompted theoretical studies of possible mechanisms, ranging from conventional configuration mixing [5,6] to an admixture of the Δ-hole (Δ-h) states [7–10]. Experimental investigations into the (p, n) [11] and (n, p) [12] reactions of ^{90}Zr using the multipole decomposition (MD) technique [13] have revealed that configuration mixing effects, such as coupling to 2-particle–2-hole ($2p$-$2h$) excitations, play an important role in GT quenching, whereas Δ-h coupling has a minor role. It has also been noted that some quenching may result from tensor interaction effects that couple the GT states with the spin-quadrupole 1^+ states [14].

The SD resonance is the lowest multipolarity spin-isospin mode involving both spatial and spin degrees of freedom. MD analysis of (p, n) cross sections has identified a considerable amount of broadly distributed dipole strength at excitation energies beyond the main GT peak [15]. Recently, Yako, Sagawa, and Sakai [16] extracted the dipole components for ^{90}Zr(p, n) and ^{90}Zr(n, p) data by MD analysis. These data were acquired at incident kinetic energies of around $T_p \simeq 300$ MeV, for

which spin excitations are dominant. Therefore, the deduced components are assumed to be the SD components. The SD strengths are obtained by assuming a proportionality relation between the SD cross section and the relevant strength [17]. The experimental SD strengths are reasonably reproduced using the second-order random phase approximation (RPA) calculation by Dróżdż *et al.* [18], although the strengths at low excitation energies are significantly overestimated. It should be noted that the experimental strengths include all the SD strengths with spin-parity transfer $\Delta J^\pi = 0^-$, 1^-, and 2^-, because separation of the individual multipole contributions is difficult in the MD analysis [13]. The separated SD strengths should be useful for further theoretical investigations on the tensor interaction effects of spin-isospin SD excitations [19–22] and the neutron matter equation of state [23].

In this article, we present measurements of cross sections and analyzing powers at nine angles over the angular range of $0° \leqslant \theta_{\text{lab}} \leqslant 10°$, in addition to complete sets of polarization transfer observables D_{ij}, and induced polarizations P, at $\theta_{\text{lab}} = 0°$, $2°$, $4°$, $5.5°$, and $7°$ for the ^{208}Pb(p, n) reaction at $T_p = 296$ MeV. Distortion effects are minimized at around this incident energy [13], and thus theoretical calculations based on the distorted-wave impulse approximation (DWIA) should be reliable, due to the simple reaction mechanism. The MD technique has been extended to simultaneously treat the data for polarization observables, and this technique has been applied to the present data. The SD strengths are successfully separated into component strengths with this technique. The results are compared with theoretical calculations based on the Skyrme Hartree-Fock (HF) plus RPA approach in order to assess the multipole-dependent effect of the tensor interaction on the SD excitations [21,22]. The GT strength is also

*wakasa@phys.kyushu-u.ac.jp;   http://ne.phys.kyushu-u.ac.jp/~ wakasa

extracted, and the effects of the isovector spin-monopole (IVSM) excitations are investigated.

II. EXPERIMENTAL METHODS

Measurements were performed using a neutron time-of-flight (NTOF) system [24] at the Research Center for Nuclear Physics (RCNP) of Osaka University. The data for the polarization transfer observables, D_{NN} and D_{LL}, at $\theta_{\rm lab} = 0°$ [25] were measured using an old neutron detector and polarimeter (NPOL2) system [26], whereas all other data were measured using a new neutron detector and polarimeter (NPOL3) system [27]. The relevant experimental techniques for the NPOL2 system have been reported previously for similar polarization transfer measurements of the ^{90}Zr(p, n) reaction at $\theta_{\rm lab} = 0°$ [28]. Thus, only a brief description of the NPOL3 system is given and experimental details relevant to the present experiments are discussed.

A. Polarized proton beam

The polarized proton beam produced by a high-intensity polarized ion source (HIPIS) [29] was accelerated up to $T_p = 53$ and 296 MeV using the azimuthally varying field (AVF) and ring cyclotrons, respectively. The beam polarization direction was reversed every 5 s by selecting rf transitions to minimize false geometric asymmetries. In measurements of the cross section and analyzing power, one out of seven beam pulses was selected for injection into the ring cyclotron, which then yielded a beam pulse period of 454 ns. This pulse selection reduces the wraparound of slow neutrons from preceding beam pulses. In the polarization transfer measurements, pulse selection was not performed, so reasonable statistical accuracy could be achieved. Single-turn extraction from the ring cyclotron was maintained during these measurements to preserve the beam polarization.

Two superconducting solenoid magnets, SOL1 and SOL2 [24], located in the injection line from the AVF to ring cyclotron were used to precess the proton spin. Each magnet can rotate the proton spin direction from the normal direction $\hat{N}$, to the sideways direction $\hat{S}$. These two magnets were installed in front of (SOL1) and behind (SOL2) a 45° bending magnet, so that the spin precession angle in the bending magnet was approximately 85.2° for $T_p = 53$ MeV protons. Therefore, proton beams with longitudinal ($\hat{L}$) and sideways ($\hat{S}$) polarizations could be obtained at the exit of the SOL2 magnet using the SOL1 and SOL2 magnets, respectively.

The beam polarization was continuously monitored using two sets of beamline polarimeters, BLP1 and BLP2 [24], installed after the ring cyclotron. Each polarimeter consists of four conjugate-angle pairs of plastic scintillators and determines the beam polarization via ^{1}H$(\vec{p}, p)^1$H scattering in the $\hat{N}$ and $\hat{S}$ directions. A self-supporting polyethylene (CH$_2$) target with a thickness of 1.1 mg/cm^2 was used as the hydrogen target, and the elastically scattered and recoiled protons were detected in kinematical coincidence with a pair of scintillators. The BLP1 and BLP2 systems were installed in front of and behind a 98° bending magnet, respectively.

The spin precession angle in this bending magnet was approximately 231.1° for $T_p = 296$ MeV protons; therefore, all components (p_S, p_N, p_L) of the polarization vector could be simultaneously determined using the BLP1 and BLP2 systems. The typical magnitude of the beam polarization was approximately 0.59.

B. Target and neutron spin-rotation magnet

The proton beam bombarded a self-supporting ^{208}Pb ($\geqslant$99%) target with a thickness of 634 mg/cm^2 located in a beam-swinger magnet [24]. Neutrons from the target entered the time-of-flight (TOF) tunnel and were detected using the NPOL3 system. Protons downstream of the target were swept by the beam swinger magnet and stopped by a graphite beam dump (Faraday cup), from which the beam current was measured. Typical beam currents used for the cross-section and polarization transfer measurements were 30 and 500 nA, respectively. The reaction angle was changed by repositioning the target along the beam trajectory inside the beam-swinger magnet.

A dipole magnet for neutron spin rotation (NSR magnet [24]) was positioned at the entrance of the TOF tunnel. The magnet was used to precess the neutron polarization vector from the longitudinal direction $\hat{L}'$ to the normal direction $\hat{N}'$ so that the longitudinal component could be measured using NPOL3 as the normal component. The NSR magnet was also used for measurement of the induced polarization P [30]. In this case, the neutron polarization was precessed in the $\hat{N}'$-$\hat{L}'$ plane by approximately 120°, depending on the neutron kinetic energy.

C. Neutron detector and polarimeter NPOL3

Neutrons were measured using the NPOL3 system [27] with a flight path length of 70 m. The NPOL3 system consists of three planes of neutron detectors. Each of the first two planes (HD1 and HD2) has 10 sets of one-dimensional position-sensitive plastic scintillators (BC408) with dimensions of $100 \times 10 \times 5$ cm^3, which covers an effective detection area of 1 m^2. The last plane (NC) is a two-dimensional position-sensitive plastic scintillator with dimensions of $100 \times 100 \times 10$ cm^3. The HD1 and HD2 planes serve as both neutron detectors and neutron polarization analyzers for the cross-section and polarization transfer measurements, respectively, and the NC plane acts as a catcher for particles scattered by the HD1 or HD2 planes.

III. DATA REDUCTION

A. Neutron detection efficiency

The neutron detection efficiency of the NPOL3 system (HD1 and HD2) was measured using the neutrons obtained from the ^{7}Li$(p, n)^7$Be(g.s. + 0.43 MeV) reaction at $\theta_{\rm lab} = 0°$, which has a constant center-of-mass cross section of $\sigma_{\rm c.m.} = 27.0 \pm 0.8$ mb/sr over a wide incident energy range of $T_p = 80$–795 MeV [31]. A self-supporting ^{7}Li (99.97% ^{7}Li)

target with a thickness of 59.4 mg/cm^2 was used. The resulting efficiency was 0.043 ± 0.002, with the overall uncertainty mainly arising from uncertainties in the cross section and thickness of the ^{7}Li target.

B. Effective analyzing power

The neutron polarization was analyzed by monitoring $\vec{n} + p$ scattering at either the HD1 or HD2 neutron detectors, and the recoiled protons were detected using the NC neutron detector. The effective analyzing power $A_{y;\text{eff}}$ of the NPOL3 system was determined using polarized neutrons from GT transitions in the ^{2}H$(p, n)pp$ and ^{12}C$(p, n)^{12}$N(g.s., 1^+) reactions at $T_p =$ 296 MeV and $\theta_{\text{lab}} = 0°$. Two types of polarized protons with normal (p_N) or longitudinal (p_L) polarizations were used. The corresponding neutron polarizations at $0°$ then become $p'_N = p_N D_{NN}(0°)$ and $p'_L = p_L D_{LL}(0°)$, respectively. The resulting asymmetries measured with NPOL3 are given by

$$\epsilon_N = p'_N A_{y;\text{eff}} = p_N D_{NN}(0°)A_{y;\text{eff}}, \quad (1a)$$

$$\epsilon_L = p'_L A_{y;\text{eff}} = p_L D_{LL}(0°)A_{y;\text{eff}}. \quad (1b)$$

The polarization transfer observables for the GT transition satisfy [28]

$$2D_{NN}(0°) + D_{LL}(0°) = -1, \quad (2)$$

so that $A_{y;\text{eff}}$ can be expressed in terms of Eqs. (1) and (2) as

$$A_{y;\text{eff}} = -\left(2\frac{\epsilon_N}{p_N} + \frac{\epsilon_L}{p_L}\right). \quad (3)$$

Therefore, $A_{y;\text{eff}}$ can be obtained without already knowing the values of $D_{ii}(0°)$. The result was $A_{y;\text{eff}} = 0.120 \pm 0.005$, in which the uncertainty is the systematic uncertainty estimated from the difference between the results for ^{2}H$(p, n)pp$ and ^{12}C$(p, n)^{12}$N(g.s., 1^+).

The $D_{LL}(0°)$ values of the ^{2}H$(p, n)pp$ reaction at $T_p =$ 305–788 MeV have been reported by McNaughton *et al.* [32], and the results are shown in Fig. 1 (open circles). The solid curve is the result obtained by fitting with a second-order polynomial. The $D_{LL}(0°)$ value at $T_p = 296$ MeV, which is determined from Eq. (1b) using the obtained $A_{y;\text{eff}}$ value, is indicated in Fig. 1 by the filled square. The $D_{LL}(0°)$ value is consistent with the energy dependence predicted using previous data, which demonstrates the reliability of the calibrations.

IV. RESULTS

A. Cross section and analyzing power

The cross-section and analyzing-power data for the ^{208}Pb(p, n) reaction at $T_p = 296$ MeV are presented in Figs. 2 and 3. The GT giant resonance with an angular-momentum transfer of $\Delta L = 0$ is prominent in the spectra for angles $\theta_{\text{lab}} \lesssim 2°$, whereas the SD resonance with $\Delta L = 1$ dominates at $\theta_{\text{lab}} = 4°$. These resonances are in the low energy transfer region of $\omega \lesssim 30$ MeV and are prominent at forward angles. In

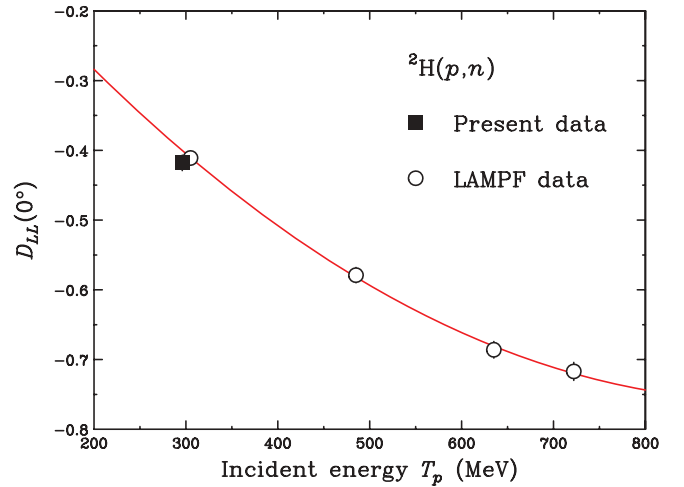FIG. 1. (Color online) Polarization transfer observables $D_{LL}(0°)$ for the ^{2}H(p, n) reaction at $0°$ as a function of incident energy T_p. The filled square indicates the present result and the open circles represent data from McNaughton *et al.* [32]. The solid curve is a fit of the data using a second-order polynomial.

the high energy transfer region, featureless continuum spectra extend up to an energy transfer of $\omega = 50$ MeV.

For the analyzing-power data, the effect of the GT giant resonance contribution is clearly observed in the spectra at $\theta_{\text{lab}} \simeq 2°$ as a negative bump at $\omega \simeq 18$ MeV, whereas that of the SD resonance is evident as a positive bump at $\omega \simeq 25$ MeV. The analyzing powers increase with the reaction angle in the continuum beyond the resonance region and reach a value of approximately 0.1 at $\theta_{\text{lab}} = 10°$.

B. Polarization transfer and induced polarization

Figures 4–6 show complete sets of polarization transfer observables D_{ij} and induced polarizations P for the ^{208}Pb(p, n) reaction at $\theta_{\text{lab}} = 0°$, $2°$, $4°$, $5.5°$, and $7°$. The data have been sorted into 1 MeV bins to reduce statistical fluctuations. The statistical uncertainties in D_{ij} are approximately 0.02–0.03 in the GT and SD resonance regions. An interesting feature of the $D_{ii}(0°)$ data is that negative values are obtained over the entire energy transfer region, which indicates a predominance of spin-flip excitations. The observed spin-flip dominance at $T_p \simeq 300$ MeV is consistent with previous studies on ^{90}Zr [28] and ^{12}C [33].

Another interesting feature of the data is the energy transfer dependence of the D_{ij} values. It should be noted that polarization transfer observables are sensitive to the spin-parity of an excited state [34], as was demonstrated for SD excitations in ^{12}N [33] and ^{16}F [35]. Thus, these data are useful for decomposition of the SD transitions into individual spin-parity components, as discussed later.

V. ANALYSIS

In this section, the experimental data are compared with the DWIA calculations employing RPA response functions
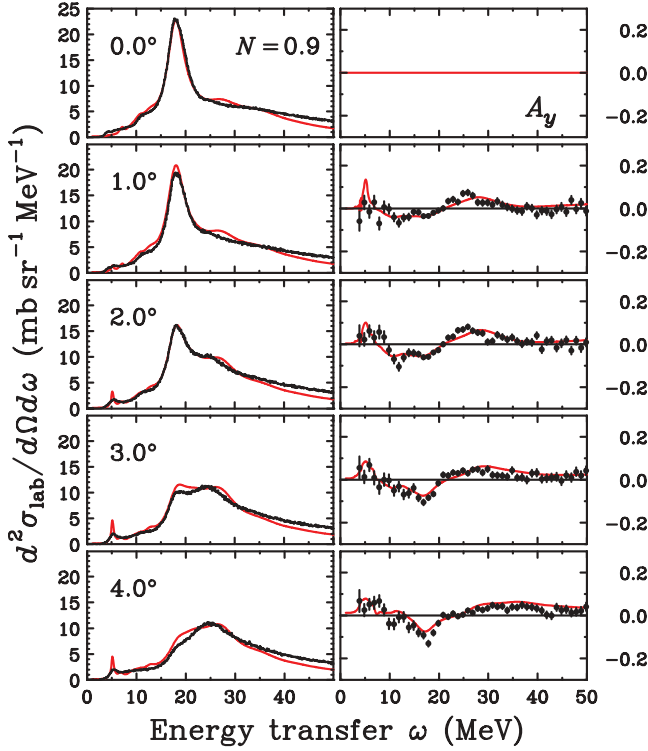
FIG. 2. (Color online) Cross sections (left panels) and analyzing powers (right panels) for the ^{208}Pb(p, n) reaction at $T_p = 296$ MeV and $\theta_{\text{lab}} = 0°$–$4°$. The cross sections and analyzing powers are binned in steps of 0.1 and 1 MeV, respectively. The solid curves show the results of DWIA calculations employing RPA response functions.

(DWIA + RPA) to investigate the distributions of the GT and SD excitations. The numerical calculations were performed using the CRDW computer code [36].

A. Random phase approximation formalism

We followed the RPA formalism described in Refs. [36, 37]. Here, the spin response functions are calculated using a continuum RPA with the ring approximation including Δ degrees of freedom. The $\pi + \rho + g'$ model interaction $V_{\text{eff}}^{\sigma\tau}$, was employed as an effective interaction and is expressed as [13]

$$V_{\text{eff}}^{\sigma\tau}(\mathbf{q}, \omega) = V_L^{\sigma\tau}(\mathbf{q}, \omega) + V_T^{\sigma\tau}(\mathbf{q}, \omega), \tag{4}$$

where the spin-longitudinal and spin-transverse terms, $V_L^{\sigma\tau}$ and $V_T^{\sigma\tau}$, are given by

$$V_L^{\sigma\tau}(\mathbf{q}, \omega) = \frac{f_{\pi NN}^2}{m_\pi^2}\left(g'_{NN} + \Gamma_{\pi NN}^2(q, \omega)\frac{q^2}{\omega^2 - q^2 - m_\pi^2}\right)$$
$$\times (\boldsymbol{\sigma}_1 \cdot \hat{\mathbf{q}})(\boldsymbol{\sigma}_2 \cdot \hat{\mathbf{q}})(\boldsymbol{\tau}_1 \cdot \boldsymbol{\tau}_2)$$
$$+ \frac{f_{\pi NN}f_{\pi N\Delta}}{m_\pi^2}\left(g'_{N\Delta} + \Gamma_{\pi NN}(q, \omega)\Gamma_{\pi N\Delta}(q, \omega)\right.$$
$$\left.\times \frac{q^2}{\omega^2 - q^2 - m_\pi^2}\right)$$
$$\times \{[(\boldsymbol{\sigma}_1 \cdot \hat{\mathbf{q}})(\mathbf{S}_2 \cdot \hat{\mathbf{q}})(\boldsymbol{\tau}_1 \cdot \mathbf{T}_2) + (1 \leftrightarrow 2)] + \text{H.c.}\}$$

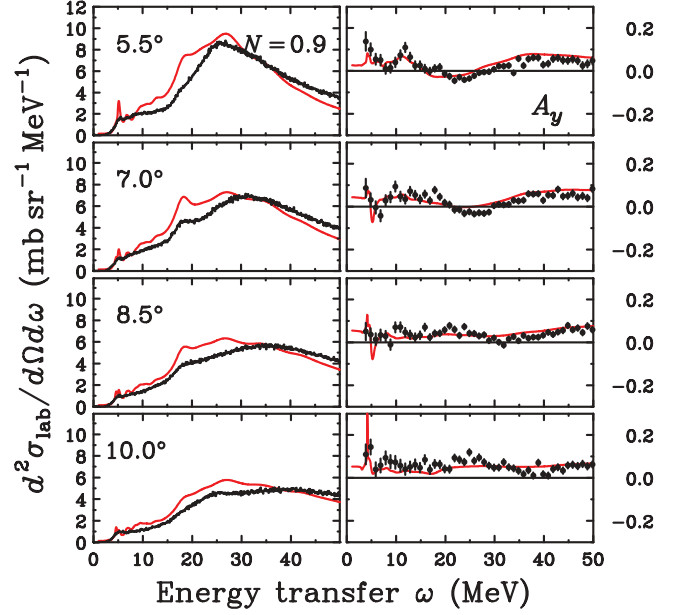FIG. 3. (Color online) As described in Fig. 2 for the range of $\theta_{\text{lab}} = 5.5°$–$10°$.

$$+ \frac{f_{\pi N\Delta}^2}{m_\pi^2}\left(g'_{\Delta\Delta} + \Gamma_{\pi N\Delta}^2(q, \omega)\frac{q^2}{\omega^2 - q^2 - m_\pi^2}\right)$$
$$\times \{[(\mathbf{S}_1 \cdot \hat{\mathbf{q}})(\mathbf{S}_2^\dagger \cdot \hat{\mathbf{q}})(\mathbf{T}_1 \cdot \mathbf{T}_2^\dagger)$$
$$+ (\mathbf{S}_1 \cdot \hat{\mathbf{q}})(\mathbf{S}_2 \cdot \hat{\mathbf{q}})(\mathbf{T}_1 \cdot \mathbf{T}_2)] + \text{H.c.}\}, \tag{5}$$

and

$$V_T^{\sigma\tau}(\mathbf{q}, \omega) = \frac{f_{\pi NN}^2}{m_\pi^2}\left(g'_{NN} + C_\rho\Gamma_{\rho NN}^2(q, \omega)\frac{q^2}{\omega^2 - q^2 - m_\rho^2}\right)$$
$$\times (\boldsymbol{\sigma}_1 \times \hat{\mathbf{q}}) \cdot (\boldsymbol{\sigma}_2 \times \hat{\mathbf{q}})(\boldsymbol{\tau}_1 \cdot \boldsymbol{\tau}_2)$$
$$+ \frac{f_{\pi NN}f_{\pi N\Delta}}{m_\pi^2}\left(g'_{N\Delta} + C_\rho\Gamma_{\rho NN}(q, \omega)\Gamma_{\rho N\Delta}(q, \omega)\right.$$
$$\left.\times \frac{q^2}{\omega^2 - q^2 - m_\rho^2}\right)$$
$$\times \{[(\boldsymbol{\sigma}_1 \times \hat{\mathbf{q}}) \cdot (\mathbf{S}_2 \times \hat{\mathbf{q}})(\boldsymbol{\tau}_1 \cdot \mathbf{T}_2)$$
$$+ (1 \leftrightarrow 2)] + \text{H.c.}\}$$
$$+ \frac{f_{\pi N\Delta}^2}{m_\pi^2}\left(g'_{\Delta\Delta} + C_\rho\Gamma_{\rho N\Delta}^2(q, \omega)\frac{q^2}{\omega^2 - q^2 - m_\rho^2}\right)$$
$$\times \{[(\mathbf{S}_1 \times \hat{\mathbf{q}}) \cdot (\mathbf{S}_2^\dagger \times \hat{\mathbf{q}})(\mathbf{T}_1 \cdot \mathbf{T}_2^\dagger)$$
$$+ (\mathbf{S}_1 \times \hat{\mathbf{q}}) \cdot (\mathbf{S}_2 \times \hat{\mathbf{q}})(\mathbf{T}_1 \cdot \mathbf{T}_2)] + \text{H.c.}\}. \tag{6}$$

Here, m_π and m_ρ are the pion- and rho-meson masses, $\boldsymbol{\sigma}$ and $\boldsymbol{\tau}$ are the spin and isospin operators of the nucleon N, and $\mathbf{S}$ and $\mathbf{T}$ are the spin and isospin transition operators, respectively, from N to Δ. The constants $f_{\pi NN}$ and $f_{\pi N\Delta}$ are the πNN and $\pi N\Delta$ coupling constants, respectively, C_ρ is the ratio of rho-meson coupling to pion coupling, and Γ_α ($\alpha = \pi NN$, $\pi N\Delta$, ρNN, and $\rho N\Delta$) are the vertex form factors. We have used the coupling constants and the meson parameters for the pion and rho-meson exchange interactions from a Bonn potential that treats Δ explicitly [38]. The peak position of
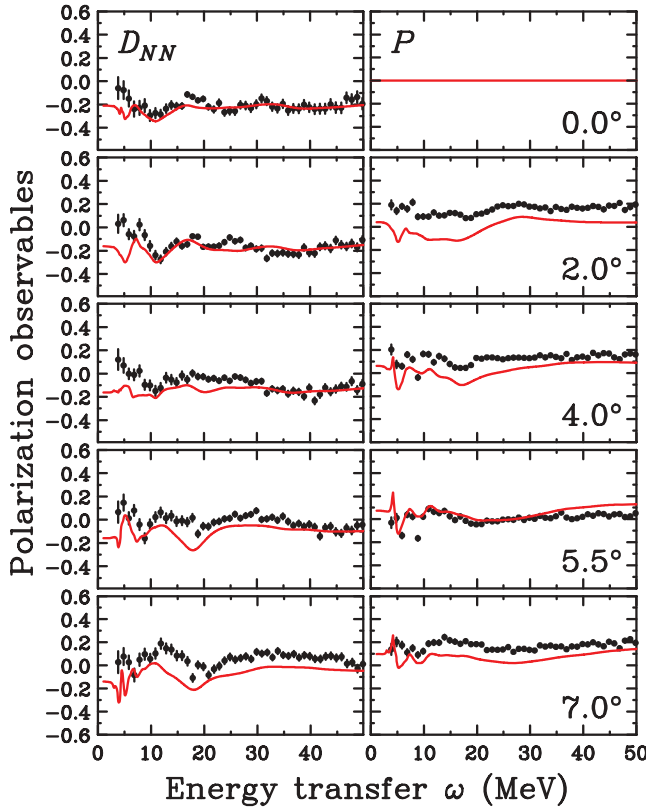
FIG. 4. (Color online) Polarization transfer observables D_{NN} (left panels) and induced polarization P (right panels) for the ^{208}Pb(p,n) reaction at $T_p = 296$ MeV and $\theta_{\text{lab}} = 0.0°$–$7.0°$. The data are binned in 1 MeV steps. The solid curves denote the results of DWIA calculations employing RPA response functions.

FIG. 5. (Color online) As described in Fig. 4, but for the polarization transfer observables $D_{S'S}$ (left panels) and $D_{L'L}$ (right panels).

the GT giant resonance is sensitive to the g'_{NN} value [39], and the present data can be well reproduced for $g'_{NN} = 0.64$. This value is consistent with previous results [39–41] and is thus used in the following calculations. The $g'_{N\Delta}$ value has been estimated to be $g'_{N\Delta} = 0.35 \pm 0.16$ based on the GT quenching factor [12]. Here, we fixed $g'_{\Delta\Delta} = 0.5$ [42], because the $g'_{\Delta\Delta}$ dependence of the results was very weak.

For the spin-scalar modes, the zero-range interaction V^{τ}_{eff}, was employed as an effective interaction and is expressed as

$$V^{\tau}_{\text{eff}} = f'\left(\frac{f^2_{\pi NN}}{m^2_{\pi}}\right)(\boldsymbol{\tau}_1 \cdot \boldsymbol{\tau}_2), \qquad (7)$$

where f' is the Landau-Migdal parameter for the spin-scalar channel. The f' value was estimated to be $f' = 0.72$ to reproduce the excitation energy $E_x = 15.2$ MeV [43] of the 0^+ isobaric-analog state (IAS) of ^{208}Bi, the present value of which is consistent with previous results [44,45].

Single-particle wave functions were generated by a Woods-Saxon (WS) potential with $r_0 = 1.27$ fm, $a_0 = 0.67$ fm, and $V_{\text{so}} = 7.5$ MeV [46]. The depths of the WS potentials for neutrons and protons were adjusted to reproduce the separation energies of the $3p_{1/2}$ and $3s_{1/2}$ orbits, respectively.
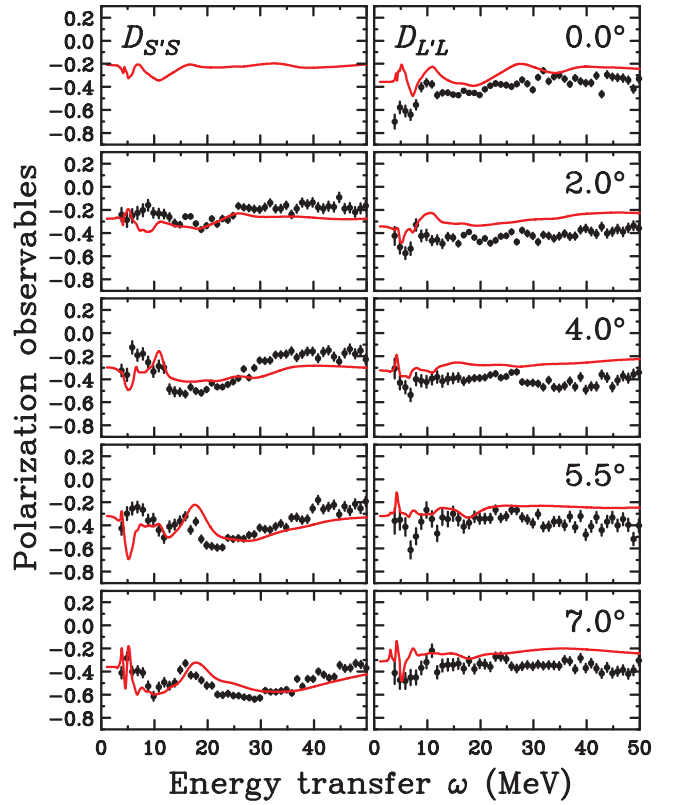
To account for many-body effects, a local effective mass approximation was adopted [30]:

$$m^*(r) = m_N - \frac{f_{\text{WS}}(r)}{f_{\text{WS}}(0)}[m_N - m^*(0)], \qquad (8)$$

where m_N is the nucleon mass and $f_{\text{WS}}(r)$ is a WS radial form. Here, we used a standard value of $m^*(0) = 0.7 m_N$ [47,48].

The spreading width of the particle states is taken into account by introducing an imaginary part to the WS potential. The phenomenological energy-dependent relation is used for the spreading width [49] given by

$$\frac{\gamma(\varepsilon)}{2} = \alpha\left[\frac{\varepsilon^2}{\varepsilon^2 + \varepsilon^2_0}\right]\left[\frac{\varepsilon^2_1}{\varepsilon^2 + \varepsilon^2_1}\right], \qquad (9)$$

where ε is measured from the single-particle energy of the outermost occupied state. The α and ε_1 values were taken from Ref. [49] as 10.75 and 110 MeV, respectively, and ε_0 is determined so as to reproduce the spectral shape of the GT giant resonance. Figure 7 compares the experimental cross section at $\theta_{\text{lab}} = 0°$ with the DWIA + RPA calculations employing three different ε_0 values. The details for the DWIA calculations are described in the next subsection. $\varepsilon_0 = 26$ MeV is adopted in the following calculations.

The depth parameter W_0, of the imaginary WS potential is set to $W_0 = \gamma(\varepsilon)/2$. The spreading width of the hole states γ_h, is also taken into account by adding an imaginary energy $i\gamma_h/2$ to the hole energy [36,50] and setting $\gamma_h = \gamma(\varepsilon)$.
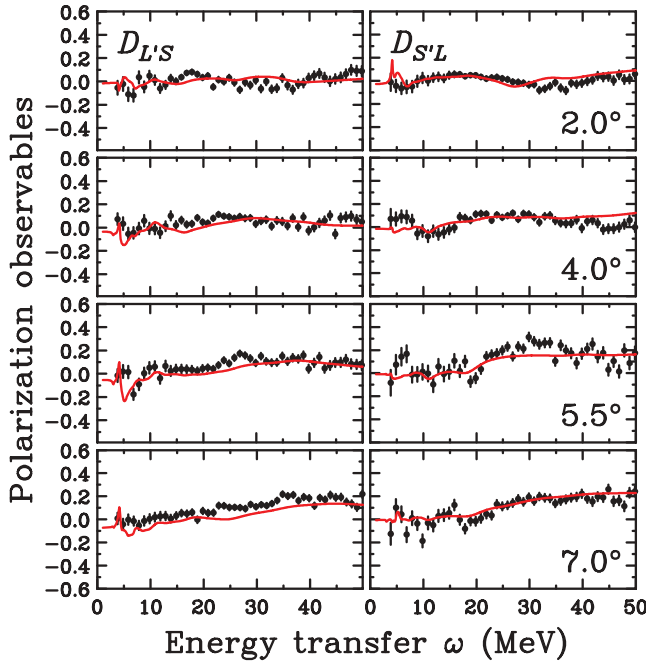
FIG. 6. (Color online) As described in Fig. 4, but for the polarization transfer observables $D_{L'S}$ (left panels) and $D_{S'L}$ (right panels) at $\theta_{\rm lab} = 2.0°–7.0°$.

B. Formalism of distorted-wave impulse approximation

We followed the DWIA formalism described in Ref. [36]. The *NN t* matrices parametrized by Franey and Love [51] were used, and interpolation was performed to deduce the *t*-matrix components at $T_p = 296$ MeV. The distorted wave for the protons was generated using a global optical model potential (OMP) in the proton energy range of $T_p = 20$–1040 MeV [52], while that for the neutrons was generated using a global OMP in the neutron energy range of $T_n = 20$–1000 MeV [53].
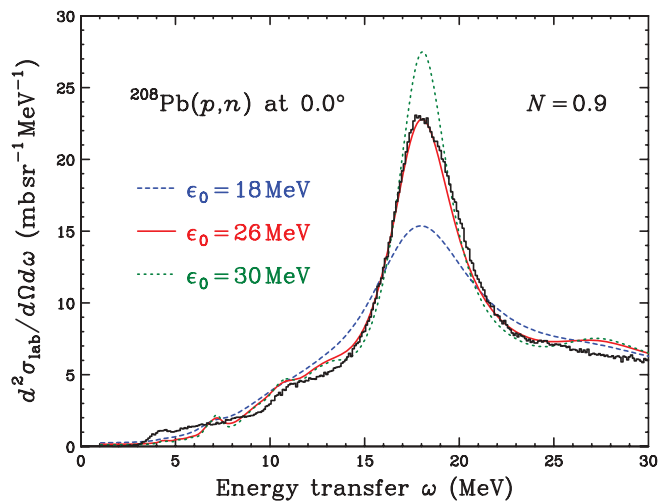

FIG. 7. (Color online) Cross sections for the ^{208}Pb(p, n) reaction at $T_p = 296$ MeV and $\theta_{\rm lab} = 0°$. The dashed, solid, and dotted curves denote the DWIA + RPA results obtained with $\epsilon_0 = 18$, 26, and 30 MeV, respectively. See text for details.
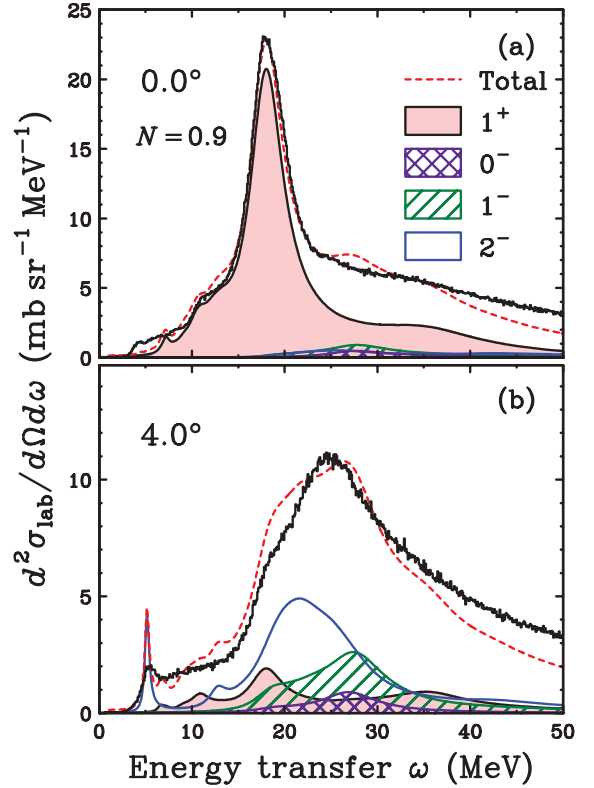

FIG. 8. (Color online) Cross sections for the ^{208}Pb(p, n) reaction at $T_p = 296$ MeV for $\theta_{\rm lab} = 0°$ (a) and $4°$ (b). The shaded, cross-hatched, hatched, and unfilled regions represent the results of DWIA + RPA calculations for the $\Delta J^\pi = 1^+$, 0^-, 1^-, and 2^- components, respectively. The dashed curves show the total cross sections, including contributions up to $\Delta J^\pi = 9^+$.

C. Comparison with DWIA + RPA calculations

The solid curves in Figs. 2 and 3 show the results of the theoretical calculations. The calculations for the cross sections shown in these figures and all following figures have been normalized by a factor of 0.9 for all ΔJ^π contributions. This factor was chosen to reproduce the GT giant resonance at $\theta_{\rm lab} = 0°$. The excess of the calculations can be redistributed [6] by mixing with $2p$-$2h$ and other excitations, which is interpreted as having significant experimental cross sections in the continuum at $\omega \gtrsim 35$ MeV. The GT resonance is reasonably reproduced in the $\theta_{\rm lab} \lesssim 2°$ spectra, whereas the SD resonance could not be well reproduced at $\theta_{\rm lab} = 4°$. Figures 8(a) and 8(b) show the contributions from the GT and SD excitations at $\theta_{\rm lab} = 0°$ and $4°$, respectively. The shaded, cross-hatched, hatched, and unfilled regions correspond to the $\Delta J^\pi = 1^+, 0^-$, 1^-, and 2^- components, respectively. The total cross sections, including components up to $\Delta J^\pi = 9^+$, are shown by the dashed curves. The peak positions of the SD resonances are expected to be multipole dependent, and thus the calculated total spectrum at $\theta_{\rm lab} = 4°$ has a broad bump. The difference between the experimental and theoretical results suggests that the multipole dependence of the SD distributions differs from the present prediction, which is investigated in Sec. VI using
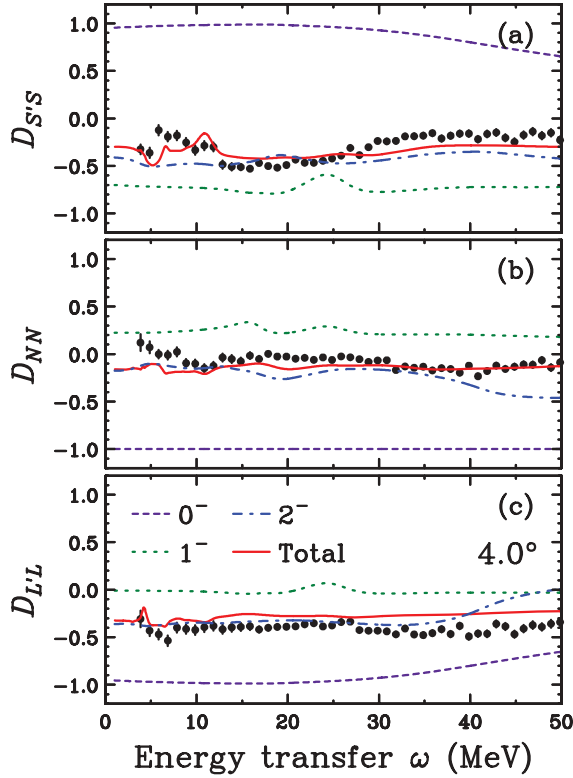
FIG. 9. (Color online) Polarization transfer observables (a) $D_{S'S}$, (b) D_{NN}, and (c) $D_{L'L}$ for the ^{208}Pb(p, n) reaction at $T_p = 296$ MeV and $\theta_{\text{lab}} = 4°$. The dashed, dotted, and dot-dashed curves represent the results of DWIA + RPA calculations for the $\Delta J^\pi = 0^-$, 1^-, and 2^- components, respectively. The solid curves show the total D_{ij}, including contributions up to $\Delta J^\pi = 9^+$.

MD analysis. We also note that the calculations predict a significant $\Delta J^\pi = 1^+$ contribution at $\omega \simeq 35$ MeV from the $(2\hbar\omega)$ IVSM transition, which has a forward-peaking angular distribution similar to that of the GT transition. Other excitations would also have contributions in this continuum region, so that the MD technique will be applied to extract the $\Delta J^\pi = 1^+$ component.

The solid curves in Figs. 4–6 show the results of calculations for the polarization transfer observables D_{ij} and induced polarizations P. The calculations reproduce the D_{NN} data fairly well at forward angles of $\theta_{\text{lab}} = 0°$ and $2°$, but do not agree well with the $D_{S'S}$ and $D_{L'L}$ data. For $D_{L'S}$ and $D_{S'L}$, the calculations reasonably reproduce the data at all angles. Polarization observables are sensitive to the spin-parity of an excited state [34]; therefore, the disagreement between the experimental and theoretical results suggests that the spin-parity composition may be slightly different from that predicted in the present RPA. Figure 9 shows typical polarization transfer observables for the $\Delta J^\pi = 0^-$, 1^-, and 2^- SD excitations at $\theta_{\text{lab}} = 4°$, at which angle the SD resonances are predominantly excited. The polarization transfer observables take distinct values depending on ΔJ^π. To investigate the reason for this discrepancy, the cross section was separated into polarized cross sections using the polarization observables.

D. Polarized cross section

The double differential cross section I ($d^2\sigma_{\text{lab}}/d\Omega d\omega$ in Figs. 2 and 3) can be separated into nonspin ID_0, spin-longitudinal ID_q, and two spin-transverse, ID_n and ID_p, polarized cross sections as follows:

$$I = ID_0 + ID_q + ID_n + ID_p, \quad (10)$$

where D_i are the polarization observables introduced by Bleszynski et al. [54]. The center-of-mass (c.m.) coordinate system, (q, n, p), in this case is defined as $\hat{\mathbf{q}} = \mathbf{q}/|\mathbf{q}|$, $\hat{\mathbf{n}} = (\mathbf{k} \times \mathbf{k}')/(|\mathbf{k} \times \mathbf{k}'|)$, and $\hat{\mathbf{p}} = \hat{\mathbf{q}} \times \hat{\mathbf{n}}$ with $\mathbf{q} = \mathbf{k}' - \mathbf{k}$, where $\mathbf{k}$ and $\mathbf{k}'$ are the momenta of the incident and outgoing nucleons, respectively, in the c.m. frame. The D_i values are related to D_{ij} in the laboratory frame as [55]

$$D_0 = \tfrac{1}{4}[1 + D_{NN} + (D_{S'S} + D_{L'L})\cos\alpha_1 \\ + (D_{L'S} - D_{S'L})\sin\alpha_1], \quad (11a)$$

$$D_n = \tfrac{1}{4}[1 + D_{NN} - (D_{S'S} + D_{L'L})\cos\alpha_1 \\ - (D_{L'S} - D_{S'L})\sin\alpha_1], \quad (11b)$$

$$D_q = \tfrac{1}{4}[1 - D_{NN} + (D_{S'S} - D_{L'L})\cos\alpha_2 \\ - (D_{L'S} + D_{S'L})\sin\alpha_2], \quad (11c)$$

$$D_p = \tfrac{1}{4}[1 - D_{NN} - (D_{S'S} - D_{L'L})\cos\alpha_2 \\ + (D_{L'S} + D_{S'L})\sin\alpha_2], \quad (11d)$$

where $\alpha_1 \equiv \theta_{\text{lab}} + \Omega$ and $\alpha_2 \equiv 2\theta_p - \theta_{\text{lab}} - \Omega$. The angle θ_p represents the angle between $\hat{\mathbf{k}}$ and $\hat{\mathbf{p}}$, and Ω is the the relativistic spin rotation angle defined in Ref. [55]. Here, we also use the spin-longitudinal ID_L and spin-transverse ID_T polarized cross sections defined as [33]

$$ID_L \equiv ID_q, \quad (12a)$$

$$ID_T \equiv ID_n + ID_p. \quad (12b)$$

Figure 10 compares the experimental ID_L and ID_T polarized cross sections with those predicted from the DWIA + RPA calculations. The shaded, cross-hatched, hatched, and unfilled regions represent the $\Delta J^\pi = 1^+$, 0^-, 1^-, and 2^- components, respectively. The total ID_i spectra, including components up to $\Delta J^\pi = 9^+$, are shown by the dashed curves. The spin-longitudinal cross section ID_L consists mainly of unnatural-parity transitions $\Delta J^\pi = 0^-$, 1^+, 2^-, etc., whereas the spin-transverse cross section ID_T consists of both natural- and unnatural-parity transitions [34,35]. Note that the unnatural-parity $\Delta J^\pi = 0^-$ transition is a special case and contributes only to ID_L. The GT giant resonance at $\omega \simeq 18$ MeV is observed in both the ID_L and ID_T spectra at $\theta_{\text{lab}} \lesssim 2°$, which is consistent with the theoretical predictions. The calculations predict a bump in the ID_L spectra at $\omega \simeq 27$ MeV, which corresponds to the $\Delta J^\pi = 0^-$ SD resonance. However, the experimental data do not show a clear bump in this region, and thus the excitation energy is likely to be different than that predicted. The magnitudes of the SD resonances are reasonably reproduced in both the ID_L and ID_T spectra at $\theta_{\text{lab}} = 4°$, whereas the energy-transfer dependence is slightly different. The discrepancies observed in the ID_L and ID_T spectra suggest that the SD strength
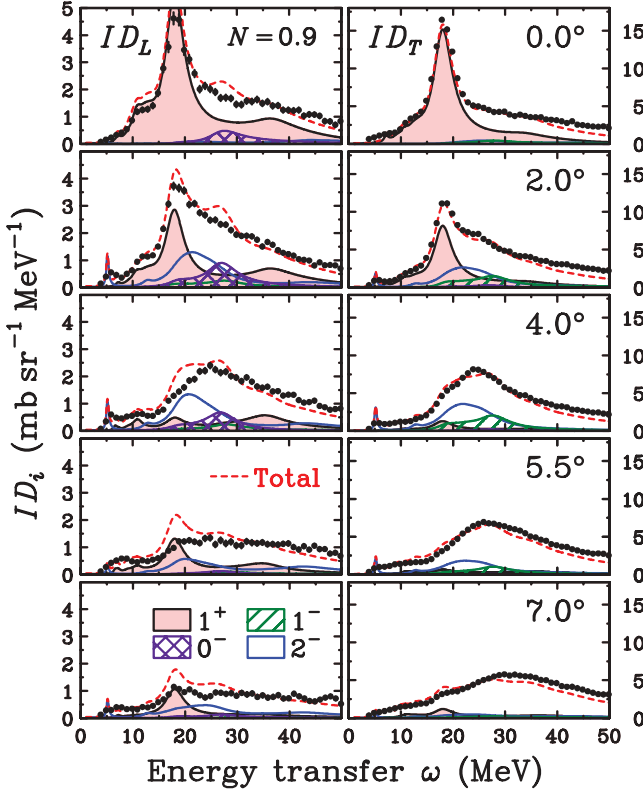
FIG. 10. (Color online) Spin-longitudinal ID_L (left panels) and spin-transverse ID_T (right panels) polarized cross sections for the ^{208}Pb(p,n) reaction at $T_p = 296$ MeV and $\theta_{lab} = 0.0°$–$7.0°$. The shaded, cross-hatched, hatched, and unfilled regions represent the results of DWIA + RPA calculations for the $\Delta J^\pi = 1^+, 0^-, 1^-$, and 2^- components, respectively. The dashed curves show the total ID_i, including contributions up to $\Delta J^\pi = 9^+$.

distributions of $\Delta J^\pi = 1^-$ and 2^- would be softened (shift toward lower energy transfer) and hardened (shift toward higher energy transfer), respectively, in comparison with those predicted by the present calculations. Therefore, MD analysis is conducted using the polarized cross sections to separate the SD resonances into individual ΔJ^π components.

VI. DISCUSSION

A. Multipole decomposition analysis

The GT [11,12] and SD [16] strengths for ^{90}Zr were successfully obtained by applying a MD technique [13] to the experimental data for the ^{90}Zr(p,n) and ^{90}Zr(n,p) reactions. The same technique has also been applied to the data for the ^{48}Ca(p,n) and ^{48}Ti(n,p) reactions to deduce the GT strengths in ^{48}Sc [56]. The SD transitions consist of contributions from the three spin-parity components of $\Delta J^\pi = 0^-, 1^-$, and 2^-. However, the SD strengths were not separated into individual ΔJ^π contributions in previous studies on ^{90}Zr. This is mainly because the angular distribution of the cross section used in the MD analysis is relatively insensitive to ΔJ^π contributions with the same ΔL [13]. However, recent theoretical investigations [19–22] suggest

that the effect of the tensor interaction on the SD strengths is dependent on ΔJ^π, and thus detailed experimental data on the SD strengths are required. It should be noted that the polarization observables are sensitive to ΔJ^π [34]; therefore, those of the SD transitions are also significantly different for $\Delta J^\pi = 0^-, 1^-$, and 2^-, as shown in Fig. 9. Therefore, MD analysis in the present case was conducted using not only the cross-section data, but also the polarization observable data to separate the SD strengths into individual ΔJ^π contributions as follows.

B. Extended multipole decomposition analysis

In standard MD analysis [13], the experimentally obtained angular distributions $I^{\text{expt}}(\theta, \omega)$, of the cross section are fit using the least-squares method, based on the following linear combination of the calculated angular distributions $I^{\text{calc}}_{\Delta J^\pi}(\theta, \omega)$, for various spin-parity transfers, ΔJ^π; that is,

$$I^{\text{expt}}(\theta, \omega) = \sum_{\Delta J^\pi} a_{\Delta J^\pi}(\omega) I^{\text{calc}}_{\Delta J^\pi}(\theta, \omega), \qquad (13)$$

where $a_{\Delta J^\pi}(\omega)$ are the fitting coefficients. The $I^{\text{calc}}_{\Delta J^\pi}(\theta, \omega)$ values are obtained from the DWIA calculations. In the presently proposed extended MD analysis, the experimental polarized cross sections, ID^{expt}_i $(i = 0, L, T)$, are fit using a linear combination of the calculated ID^{calc}_i values as

$$ID^{\text{expt}}_i(\theta, \omega) = \sum_{\Delta J^\pi} a_{\Delta J^\pi}(\omega) ID^{\text{calc}}_{i;\Delta J^\pi}(\theta, \omega). \qquad (14)$$

For $\Delta J^\pi = 1^-$, the spin-scalar (spin-transfer $\Delta S = 0$) and spin-vector ($\Delta S = 1$) components are treated separately.

The analyzing power $A^{\text{calc}}_y(\theta, \omega)$, is also obtained from the DWIA results, $A^{\text{calc}}_{y;\Delta J^\pi}(\theta, \omega)$, by weighting each ΔJ^π contribution, $a_{\Delta J^\pi}(\omega) I^{\text{calc}}_{\Delta J^\pi}(\theta, \omega)$:

$$A^{\text{calc}}_y(\theta, \omega) = \frac{\sum_{\Delta J^\pi} a_{\Delta J^\pi}(\omega) I^{\text{calc}}_{\Delta J^\pi}(\theta, \omega) A^{\text{calc}}_{y;\Delta J^\pi}(\theta, \omega)}{\sum_{\Delta J^\pi} a_{\Delta J^\pi}(\omega) I^{\text{calc}}_{\Delta J^\pi}(\theta, \omega)}. \qquad (15)$$

The experimental analyzing powers $A^{\text{expt}}_y(\theta, \omega)$, are also fit using $A^{\text{calc}}_{y;\Delta J^\pi}(\theta, \omega)$. However, because the number of data points is limited, the transitions having $\Delta J^\pi \geqslant 4^-$ are divided into two groups corresponding to the natural- and unnatural-parity transitions. Thus, the explicit expression of Eq. (14) is given with twelve fitting coefficients $a_{\Delta J^\pi}(\omega)$ as

$$\begin{aligned}
ID^{\text{expt}}_i(\theta, \omega) = {} & a_{0^+}(\omega) ID^{\text{calc}}_{i;0^+}(\theta, \omega) + a_{1^+}(\omega) ID^{\text{calc}}_{i;1^+}(\theta, \omega) \\
& + a_{0^-}(\omega) ID^{\text{calc}}_{i;0^-}(\theta, \omega) \\
& + a_{1^-;\Delta S=0}(\omega) ID^{\text{calc}}_{i;1^-;\Delta S=0}(\theta, \omega) \\
& + a_{1^-;\Delta S=1}(\omega) ID^{\text{calc}}_{i;1^-;\Delta S=1}(\theta, \omega) \\
& + a_{2^-}(\omega) ID^{\text{calc}}_{i;2^-}(\theta, \omega) \\
& + a_{2^+}(\omega) ID^{\text{calc}}_{i;2^+}(\theta, \omega) + a_{3^+}(\omega) ID^{\text{calc}}_{i;3^+}(\theta, \omega) \\
& + a_{3^-}(\omega) ID^{\text{calc}}_{i;3^-}(\theta, \omega) + a_{4^-}(\omega) ID^{\text{calc}}_{i;4^-}(\theta, \omega) \\
& + a_{J^\pi \geqslant 4^+}(\omega) ID^{\text{calc}}_{i;J^\pi \geqslant 4^+}(\theta, \omega) \\
& + a_{J^\pi \geqslant 5^-}(\omega) ID^{\text{calc}}_{i;J^\pi \geqslant 5^-}(\theta, \omega), \qquad (16)
\end{aligned}$$

where $a_{1^-;\Delta S=0}(\omega)ID^{calc}_{i;1^-;\Delta S=0}(\theta,\omega)$ and $a_{1^-;\Delta S=1}(\omega)ID^{calc}_{i;1^-;\Delta S=1}(\theta,\omega)$ are the spin-scalar and spin-vector components for $\Delta J^\pi = 1^-$, respectively.

The χ^2 value in the fitting procedure is defined as

$$\chi^2 = \sum_{\theta_j=\{\Theta\}} \left(\frac{I^{expt}(\theta_j) - I^{calc}(\theta_j)}{\delta I(\theta_j)} \right)^2$$
$$+ \sum_{i=0,L,T} \sum_{\theta_j=\{\Phi\}} \left(\frac{ID^{expt}_i(\theta_j) - ID^{calc}_i(\theta_j)}{\delta ID_i(\theta_j)} \right)^2$$
$$+ \sum_{\theta_j=\{\Psi\}} \left(\frac{A^{expt}_y(\theta_j) - A^{calc}_y(\theta_j)}{\delta A_y(\theta_j)} \right)^2, \qquad (17)$$

with

$$\delta I(\theta_j) = \max[\delta I^{expt}(\theta_j), \alpha \times I^{expt}(\theta_j)], \qquad (18a)$$
$$\delta ID_i(\theta_j) = \max\left[\delta ID^{expt}_i(\theta_j), \alpha \times ID^{expt}_i(\theta_j)\right], \qquad (18b)$$
$$\delta A_y(\theta_j) = \max[\delta A^{expt}_y(\theta_j), \alpha], \qquad (18c)$$

where $\delta I^{expt}(\theta_j)$, $\delta ID^{expt}_i(\theta_j)$, and $\delta A^{expt}_y(\theta_j)$ are the statistical uncertainties of $I^{expt}(\theta_j)$, $ID^{expt}_i(\theta_j)$, and $A^{expt}_y(\theta_j)$, respectively. Here, we take $\alpha = 0.03$ [57] to avoid trapping in an unphysical local χ^2 minimum. The α dependence of the final results was also investigated in the range of $\alpha \leqslant 0.06$ with consideration of the systematic uncertainties in the data. The angle groups, $\{\Theta\}$, $\{\Phi\}$, and $\{\Psi\}$, are given as

$$\{\Theta\} = 1^\circ, \ 3^\circ, \ 8.5^\circ, \ 10^\circ, \qquad (19a)$$
$$\{\Phi\} = 0^\circ, \ 2^\circ, \ 4^\circ, \ 5.5^\circ, \ 7^\circ, \qquad (19b)$$
$$\{\Psi\} = 1^\circ, \ 2^\circ, \ 3^\circ, \ 4^\circ, \ 5.5^\circ, \ 7^\circ, \ 8.5^\circ, \ 10^\circ. \qquad (19c)$$

The variables $a_{\Delta J^\pi}(\omega)$ in Eq. (16) are determined using the least-squares technique with this χ^2 to simultaneously reproduce the cross-section and polarization observable data.

The DWIA calculations were performed using the same computer code CRDW [36] as used previously. The parameters in the DWIA and RPA calculations are the same as those used in the previous calculations. The calculations were performed for ΔJ^π transfers up to $\Delta J^\pi = 9^+$. In a previous MD analysis [13], the $I^{calc}_{\Delta J^\pi}(\theta, \omega)$ values for a given ΔJ^π were evaluated for several 1-particle–1-hole ($1p$-$1h$) configurations, and the $1p$-$1h$ configuration that provided the best fit to the cross-section data was selected. However, this method is not realistic for the ^{208}Pb(p, n) reaction, because the number of possible $1p$-$1h$ configurations is considerably larger than those for the ^{90}Zr(p, n) and ^{90}Zr(n, p) reactions. The present DWIA + RPA calculations provide an approximate description of the data, as shown in Sec. VC; therefore, the $I^{calc}_{\Delta J^\pi}$ values were used in these calculations.

Figures 11 and 12 show the cross sections and analyzing powers obtained by MD analysis, respectively. The cross-section results are shown with the ΔJ^π transitions grouped to the lowest dominant ΔL value in the present angular range. The results of MD analysis are in reasonable agreement
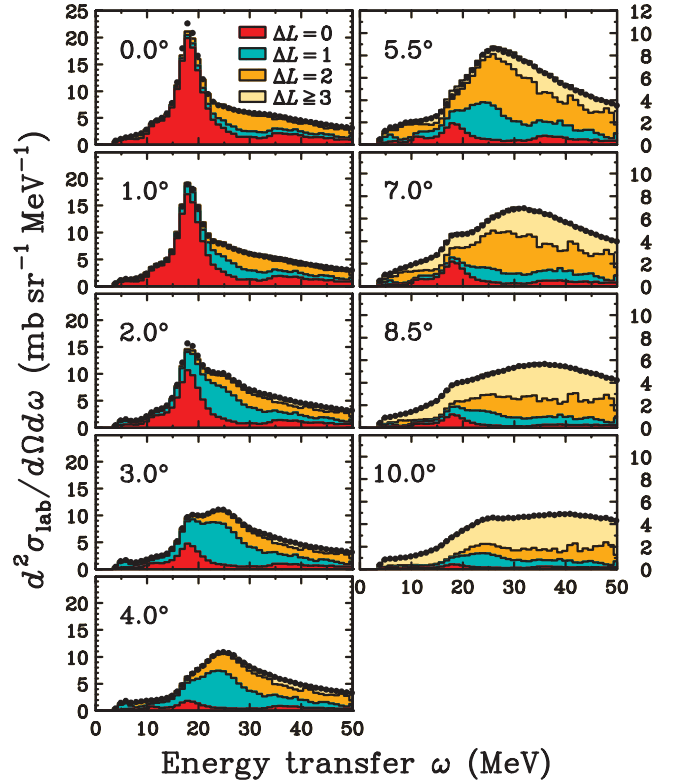

FIG. 11. (Color online) Cross-section results obtained by MD analysis. See text for details.

with the cross-section and analyzing-power data over the entire energy transfer region for all angles. The MD analysis clearly shows a fairly large contribution from the $\Delta L = 0$ component up to $\omega \simeq 50$ MeV. This $\Delta L = 0$ contribution in the continuum is due to both the configuration mixing and IVSM contributions. It should be noted that the present MD analysis provides a reasonable description for the cross section at $\theta_{lab} = 4^\circ$, which could not be realized with the DWIA + RPA calculations, as discussed in Sec. VC. In addition, a fairly large contribution from the $\Delta L = 1$ component including the SD transitions can be identified up to $\omega \simeq 50$ MeV.

Figures 13 and 14 show the polarized cross sections obtained by MD analysis. For the nonspin polarized cross sections ID_0, at $\theta_{lab} \lesssim 4^\circ$, the $\Delta J^\pi = 0^+$ IAS transition and the $\Delta J^\pi = 1^-$ giant dipole resonance (GDR) are evident at $\omega \simeq 18$ and 26 MeV, respectively. For the $\Delta J^\pi = 0^-$ SD transition, the MD results show significant strength concentrated at $\omega \simeq 32$ MeV in the ID_L data, which is significantly higher than the DWIA + RPA prediction of $\omega \simeq 27$ MeV. For the $\Delta J^\pi = 1^-$ transition, two bumps at $\omega \simeq 19$ and 25 MeV are clearly observed in the ID_T data at $\theta_{lab} = 4^\circ$, even though the DWIA + RPA calculations predict a higher energy transfer of $\omega \simeq 27$ MeV. For the $\Delta J^\pi = 2^-$ transition, the results show a broad bump at $\omega \simeq 24$ MeV in both the ID_L and ID_T data, which is slightly higher than that predicted from the DWIA + RPA calculations, as shown in Fig. 10. In the following, the experimental GT and SD strengths are derived and compared with those obtained by theoretical calculations.
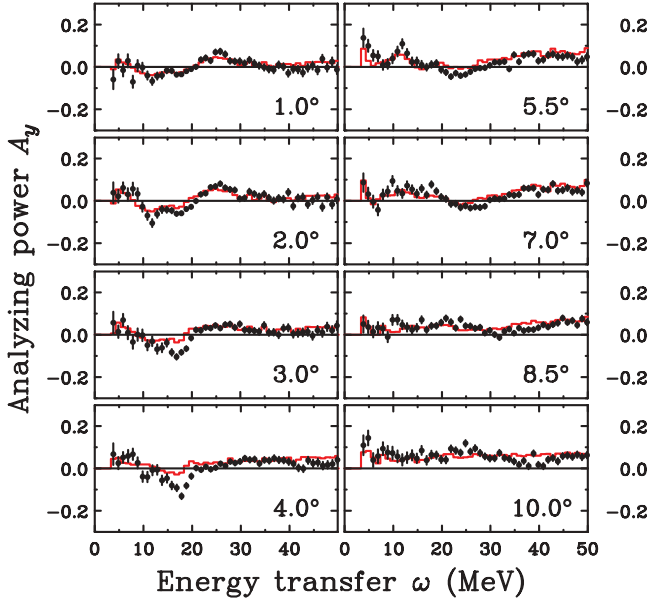
FIG. 12. (Color online) Analyzing-power results obtained by MD analysis.

C. Gamow-Teller unit cross section

The $\Delta J^\pi = 1^+$ cross section $I_{1^+}(q, \omega)$, can be related to the corresponding GT strength $B(\mathrm{GT}; \omega)$, as [13,58]

$$I_{1^+}(q, \omega) = \hat{\sigma}_{\mathrm{GT}} F(q, \omega) B(\mathrm{GT}; \omega), \qquad (20)$$

where $\hat{\sigma}_{\mathrm{GT}}$ is the GT unit cross section and $F(q, \omega)$ represents the (q, ω) dependence with a normalization of $F(0, 0) = 1$.

The $\hat{\sigma}_{\mathrm{GT}}$ values were obtained using the present DWIA calculations. These values were investigated for several nuclei from ^{12}C to ^{208}Pb, and the results for typical $1p$-$1h$ configurations, such as $(\pi 1 p_{1/2}, \nu 1 p_{3/2}^{-1})$ for ^{12}C, and $(\pi 1 i_{13/2}, \nu 1 i_{13/2}^{-1})$
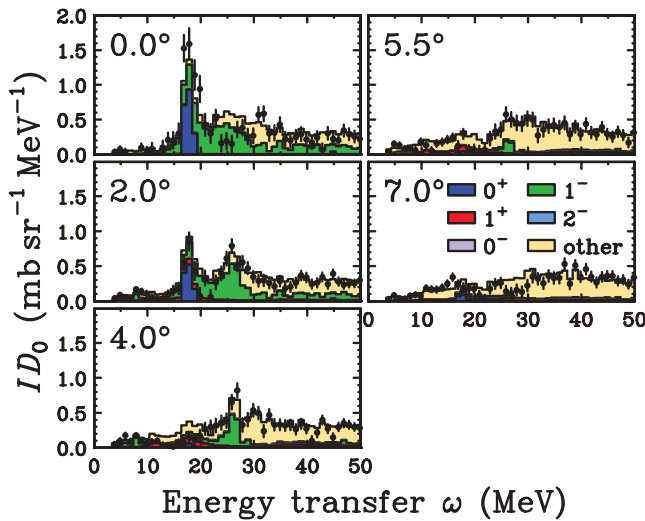

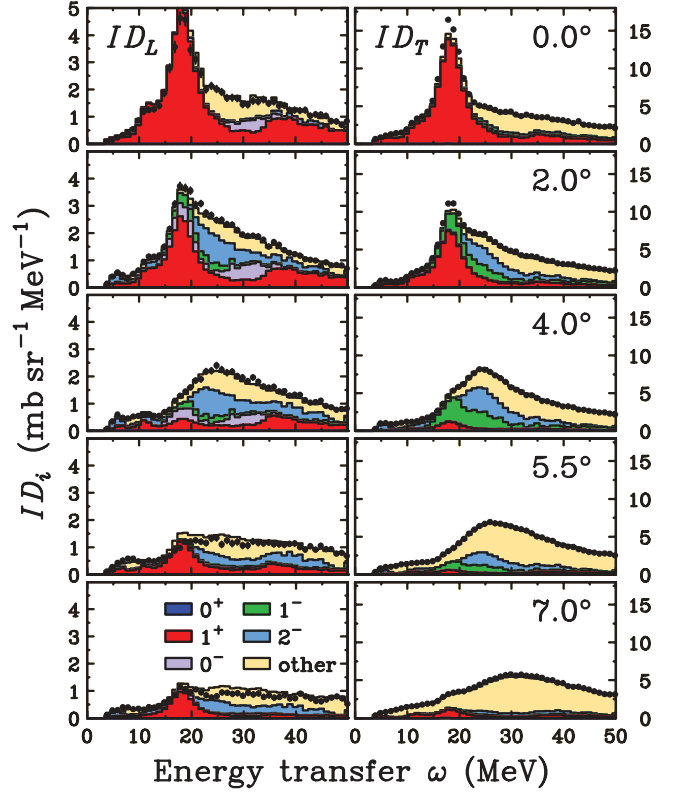FIG. 13. (Color online) Nonspin $I D_0$ polarized cross sections obtained by MD analysis.

FIG. 14. (Color online) Spin-longitudinal $I D_L$ (left panels) and spin-transverse $I D_T$ (right panels) polarized cross sections obtained by MD analysis.

and $(\pi 1 i_{11/2}, \nu 1 i_{13/2}^{-1})$ for ^{208}Pb, are shown in Fig. 15. It is assumed here that the mass-number A dependence can be written as a smooth function of A; that is,

$$\hat{\sigma}_{\mathrm{GT}}(A) = N \exp(-x A^{1/3}), \qquad (21)$$

according to the parametrization set out in Ref. [58]. Here, N represents the GT unit cross section at $A = 0$ and x is an adjustable parameter. The result of fitting with Eq. (21) is represented by the solid line in Fig. 15, which reproduces the A dependence reasonably well. The experimental $\hat{\sigma}_{\mathrm{GT}}$ values [59] (open circles) are also accurately reproduced by the present A dependence and are generally within 15% uncertainty, as shown by the band in Fig. 15. Therefore, the uncertainties of the following GT, IVSM, and SD strengths that were deduced with the help of the present DWIA calculations are estimated to be approximately 15%.

D. Gamow-Teller and isovector spin monopole strengths

The $\Delta J^\pi = 1^+$ cross section, $a_{1^+}(\omega) I_{1^+}^{\mathrm{calc}}(\theta, \omega)$, in the MD analysis contains not only the GT contribution, but also other contributions such as those from the IVSM transition. In the present analysis, it was assumed that the relative contributions from GT and IVSM transitions were the same as those of the DWIA + RPA calculations. The experimental GT and IVSM strengths, $B(\mathrm{GT}; \omega)$ and $B(\mathrm{IVSM}; \omega)$, can therefore
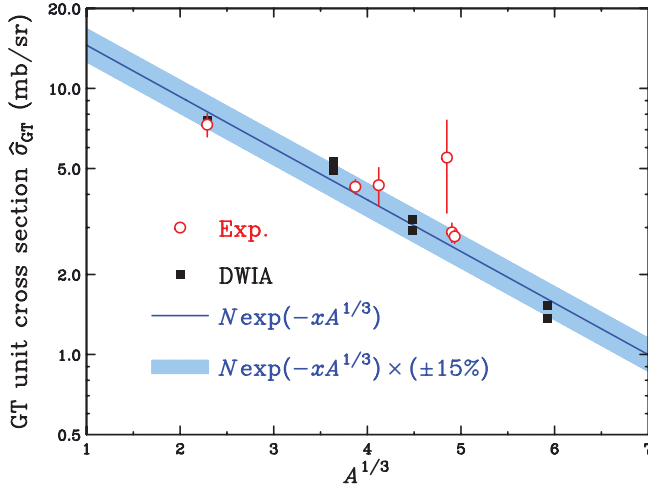
FIG. 15. (Color online) Gamow-Teller unit cross sections $\hat{\sigma}_{GT}$ as a function of $A^{1/3}$. The open circles show the experimental data taken from Ref. [59] and the filled squares represent the DWIA predictions for typical nuclei from ^{12}C to ^{208}Pb. The solid line represents the result of fitting with Eq. (21), and the blue band represents the estimated uncertainty of $\pm 15\%$.

be deduced as

$$B(\text{GT}; \omega) = a_{1^+}(\omega) B_{1^+}^{\text{calc}}(\text{GT}; \omega), \qquad (22a)$$

$$B(\text{IVSM}; \omega) = a_{1^+}(\omega) B_{1^+}^{\text{calc}}(\text{IVSM}; \omega), \qquad (22b)$$

where $B^{\text{calc}}(\text{GT}; \omega)$ and $B^{\text{calc}}(\text{IVSM}; \omega)$ are the theoretical GT and IVSM strengths, respectively, which are calculated using the same continuum RPA as that used to obtain $I_{1^+}^{\text{calc}}(\theta, \omega)$. The integrated GT and IVSM strengths, $S_{GT}(\omega)$ and $S_{\text{IVSM}}(\omega)$, are defined as

$$S_{GT}(\omega) = \int^{\omega} B(\text{GT}; \omega) d\omega, \qquad (23a)$$

$$S_{\text{IVSM}}(\omega) = \int^{\omega} B(\text{IVSM}; \omega) d\omega. \qquad (23b)$$

For the IVSM strength, we restrict examination to the part of the $2\hbar\omega$ compression mode, as is often done [60]. The prescription by Hamamoto and Sagawa [61] is adopted to extract $B^{\text{calc}}(\text{IVSM}; \omega)$ for this mode, thereby employing the following operator:

$$\hat{O}_{\text{IVSM}} = \sum_{k=1}^{A} t_{k;-} \boldsymbol{\sigma}_k \left[r_k^2 - \langle r^2 \rangle_{\text{excess}} \right], \qquad (24)$$

where $\langle r^2 \rangle_{\text{excess}}$ is the average value of $\langle r^2 \rangle$ for the excess neutrons and $\langle r^2 \rangle_{\text{excess}} = 47$ fm^2 is used.

Figures 16(a) and 16(b) show the $B(\text{GT}; \omega)$ and $S_{GT}(\omega)$ distributions, respectively. The bands represent the uncertainties arising from the selection of α in Eq. (18). The solid and dashed curves are the results of calculations by Drożdż et al. [18] and Dang et al. [62], respectively, both of which include configuration mixing effects. The results of calculations in these figures have been normalized by a quenching factor of $Q = 0.86$ [13]. The GT giant resonance peak calculated by
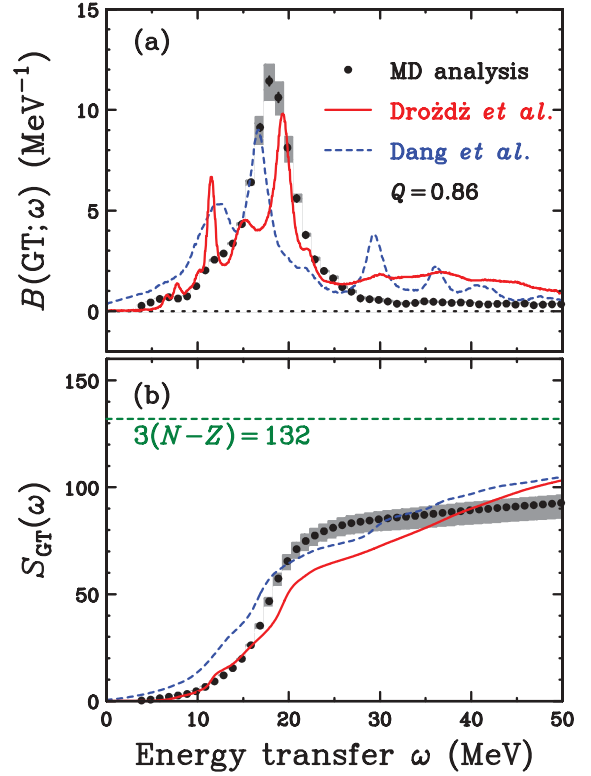

FIG. 16. (Color online) (a) The GT strength $B(\text{GT}; \omega)$ and (b) its integrated $S_{GT}(\omega)$ distributions obtained by MD analysis of the ^{208}Pb(p, n) reaction. The bands represent the uncertainties arising from the selection of α in Eq. (18). The solid and dashed curves are the theoretical predictions reported by Drożdż et al. [18] and Dang et al. [62], respectively, with a quenching factor $Q = 0.86$ [13].

Drożdż et al. is in agreement with the present result, whereas that identified by Dang et al. is slightly lower. Both theoretical distributions are significantly extended beyond the GT giant resonance region due to configuration mixing effects, and the integrated strengths are slightly larger than the present result at $\omega \simeq 50$ MeV. It should be noted that there are some sources of uncertainty, such as interference between the GT and IVSM transitions [61]. Thus, further simultaneous investigations into interference and configuration mixing effects should provide more quantitative and precise information on the GT strength.

Figures 17(a) and 17(b) show the $B(\text{IVSM}; \omega)$ and $S_{\text{IVSM}}(\omega)$ distributions, respectively. The solid curves are the present RPA predictions. The extracted peak position is approximately $\omega \simeq 37$ MeV ($E_x \simeq 35$ MeV for the excitation energy of ^{208}Bi), which is consistent with the previous values of $E_x = 32$ and 37 ± 1 MeV obtained for (p, n) [63] and $(^3\text{He}, t)$ [64] reactions, respectively. The experimental data are distributed over a wide energy region, which is also consistent with the previous results [63,64]. The integrated strength up to $\omega = 60$ MeV is almost consistent with the RPA calculation. The present $S_{\text{IVSM}}(60$ MeV$)$ value of $(6.4 \pm 0.1^{+0.2}_{-1.1}) \times 10^4$ fm^4 corresponds to $(83 \pm 2^{+3}_{-15})\%$ of $S_{\text{IVSM}} = 4\pi \times 6146 = 7.7 \times 10^4$ fm^4 [65] in the normal-mode (NM) calculation [66], which fully exhausts the non-energy-weighted sum rule. It
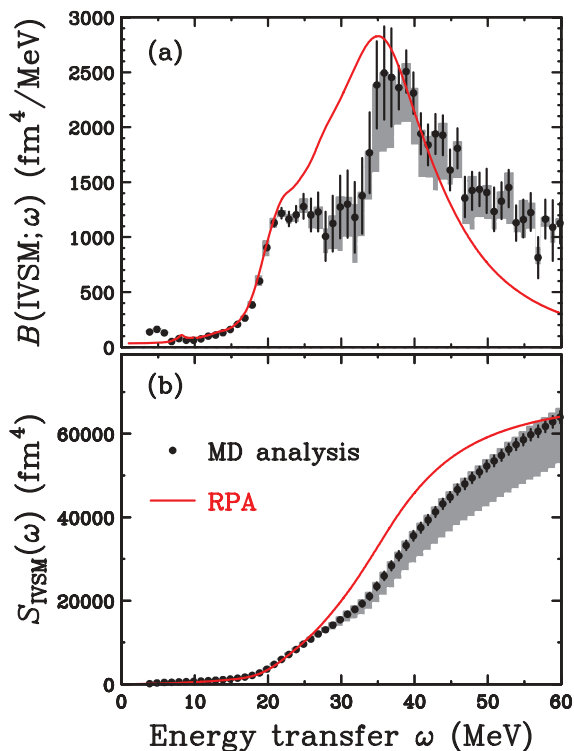
FIG. 17. (Color online) (a) The IVSM strength $B(\mathrm{IVSM};\omega)$ and (b) its integrated $S_{\mathrm{IVSM}}(\omega)$ distributions obtained by MD analysis of the $^{208}\mathrm{Pb}(p,n)$ reaction. The bands represent the uncertainties arising from the selection of α in Eq. (18). The solid curves are the predictions obtained by RPA. See text for details.

should be noted that only approximately $(60 \pm 5 \pm 14)\%$ of the NM strength was found in the study of the $(^{3}\mathrm{He}, t)$ reaction at $T_{^{3}\mathrm{He}} = 410$ MeV [64]. This discrepancy would be due to the fact that the contributions from the GT and IVSM transitions and their interference effects are significantly different for the (p, n) and $(^{3}\mathrm{He}, t)$ reactions [67]. Therefore, further theoretical investigations into interference effects are also required to resolve the discrepancy for the IVSM strength.

E. Spin dipole strength

The SD strength $B(\mathrm{SD}, \Delta J^{\pi};\omega)$, is obtained by assuming a proportionality relation [17,68] similar to that used for the GT strength. To evaluate $B(\mathrm{SD}, \Delta J^{\pi};\omega)$, the same prescription as that used in Eq. (22) for $B(\mathrm{GT};\omega)$ and $B(\mathrm{IVSM};\omega)$ is adopted, given as

$$B(\mathrm{SD}, \Delta J^{\pi};\omega) = a_{\Delta J^{\pi}}(\omega)B^{\mathrm{calc}}(\mathrm{SD}, \Delta J^{\pi};\omega), \quad (25)$$

where $B^{\mathrm{calc}}(\mathrm{SD}, \Delta J^{\pi};\omega)$ is the theoretical SD strength corresponding to $I_{\Delta J^{\pi}}^{\mathrm{calc}}(\theta, \omega)$ in the MD analysis.

Figures 18(b), 18(c), and 18(d) represent the SD strength distributions for $\Delta J^{\pi} = 0^{-}$, 1^{-}, and 2^{-}, respectively, while Fig. 18 (a) shows the total SD strength obtained as the sum of these three strengths. The error bars indicate the statistical uncertainties, while the bands represent the uncertainties arising from the selection of α in Eq. (18). The total SD strength spectrum shows a dominant resonance centered at
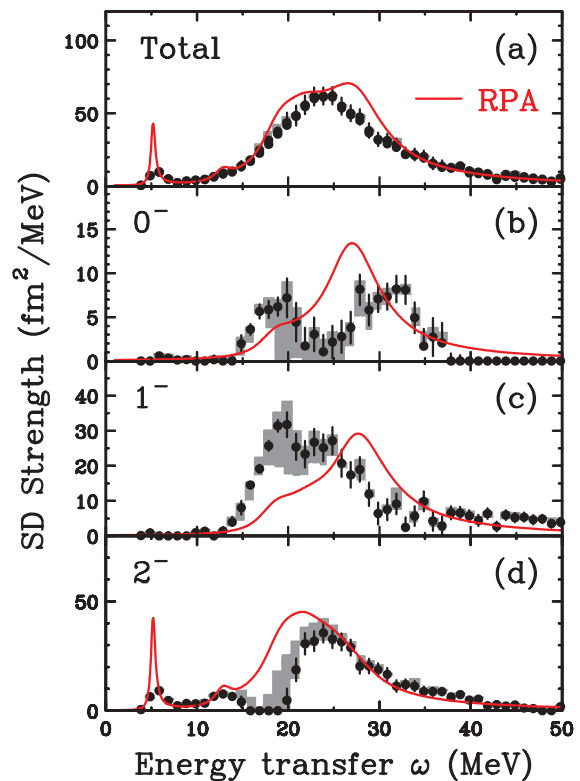

FIG. 18. (Color online) The SD strength distributions obtained by MD analysis of the $^{208}\mathrm{Pb}(p,n)$ reaction. The separated SD strengths are presented in panels (b)–(d) for $\Delta J^{\pi} = 0^{-}$, 1^{-}, and 2^{-}, respectively, and the total SD strength is shown in panel (a). The bands represent the uncertainties arising from the selection of α in Eq. (18). The solid curves are the predictions obtained by RPA.

$\omega \simeq 24$ MeV with the strength extending up to $\omega \simeq 50$ MeV. The $\Delta J^{\pi} = 2^{-}$ spectrum also shows a dominant resonance centered at $\omega \simeq 24$ MeV. In contrast, the $\Delta J^{\pi} = 1^{-}$ strength has a double-peak structure with peak energies of $\omega \simeq 19$ and 25 MeV. Similarly, the $\Delta J^{\pi} = 0^{-}$ spectrum also has a double-peak structure with peak energies at $\omega \simeq 19$ and 32 MeV. It should be noted that there are large uncertainties at $\omega \simeq 19$ MeV for all SD strengths. The asymmetric uncertainties mean that some of the $\Delta J^{\pi} = 0^{-}$ and 1^{-} strengths at $\omega \simeq 19$ MeV could be attributed to the $\Delta J^{\pi} = 2^{-}$ strength (note the scale differences of the figures).

The solid curves in Fig. 18 show the RPA predictions, which give a qualitative description of the total SD strength; however, some discrepancies are found for the separated SD strengths. The centroids of the resonances are significantly lower and higher than the experimental results for $\Delta J^{\pi} = 0^{-}$ and 1^{-}, respectively. The centroid of the $\Delta J^{\pi} = 1^{-}$ resonance is expected to be higher than that of the $\Delta J^{\pi} = 2^{-}$ resonance, because the unperturbed $1p$-$1h$ excitation energy for $\Delta J^{\pi} = 1^{-}$ is generally larger than that for $\Delta J^{\pi} = 2^{-}$. However, the present measured centroids for $\Delta J^{\pi} = 1^{-}$ and 2^{-} are very similar. In the following, we compare the present results with the self-consistent HF + RPA calculations including Skyrme interactions [22] to quantitatively investigate the effects of the tensor interaction on the SD strengths.

F. Comparison with calculations including Skyrme interactions

The parametrization of nuclear effective interactions, such as zero-range Skyrme interactions [69], has been quite successful to describe many nuclear properties [70,71]. While most of the Skyrme parameter sets are purely central, extensive efforts have recently been focused on including the noncentral tensor term [72–79]. Note that the tensor interaction is particularly crucial to understand the evolution of single-particle energies of exotic nuclei [80,81]. Recently, self-consistent HF + RPA schemes including the tensor interaction have been developed [14,82,83]. In these schemes, it is found that the tensor interaction has a characteristic ΔJ^π-dependent effect on the SD strengths [21,22]; therefore, the SD distributions are considered to play an essential role in constraining this interaction.

The triplet-even (TE) and triplet-odd (TO) zero-range tensor terms of the Skyrme interaction are expressed as [69,84]

$$
V^T = \frac{T}{2}\left\{\left[(\sigma_1 \cdot \mathbf{k}')(\sigma_2 \cdot \mathbf{k}') - \frac{1}{3}(\sigma_1 \cdot \sigma_2)\mathbf{k}'^2\right]\delta(\mathbf{r})\right.
$$
$$
+ \delta(\mathbf{r})\left[(\sigma_1 \cdot \mathbf{k})(\sigma_2 \cdot \mathbf{k}) - \frac{1}{3}(\sigma_1 \cdot \sigma_2)\mathbf{k}^2\right]\right\}
$$
$$
+ \frac{U}{2}\left\{(\sigma_1 \cdot \mathbf{k}')\delta(\mathbf{r})(\sigma_2 \cdot \mathbf{k}) + (\sigma_2 \cdot \mathbf{k}')\delta(\mathbf{r})(\sigma_1 \cdot \mathbf{k})\right.
$$
$$
\left.- \frac{2}{3}[(\sigma_1 \cdot \sigma_2)\mathbf{k}' \cdot \delta(\mathbf{r})\mathbf{k}]\right\}, \tag{26}
$$

where T and U denote the TE and TO tensor interactions, respectively.

Figure 19 compares the experimental results with the HF + RPA predictions [22]. The calculations were performed by adding the tensor terms on top of the existing interaction SGII. Three sets of tensor terms with $(T, U) = (500, -350)$, $(600, 0)$, and $(650, 200)$ have been investigated, which are labeled as SGII + Te1, SGII + Te2, and SGII + Te3, respectively. These tensor interactions have been determined to reproduce the centroids of the GT and total SD strengths for ^{90}Zr and ^{208}Pb within 2.5 MeV. All three sets of tensor terms provide reasonable descriptions for $\Delta J^\pi = 1^-$ and 2^-. The $\Delta J^\pi = 0^-$ SD distribution is sensitive to the tensor terms and the SGII + Te3 set is the most preferable of the three tensor interactions. Therefore, the present ΔJ^π-separated SD strengths provide valuable information to determine the tensor components of the Skyrme interaction.

Figure 20 compares the integrated SD strengths with the HF + RPA predictions. Here, the integrated strength $S_{SD,\Delta J^\pi}(\omega)$, is defined as

$$
S_{SD,\Delta J^\pi}(\omega) = \int^\omega B(SD, \Delta J^\pi; \omega)d\omega. \tag{27}
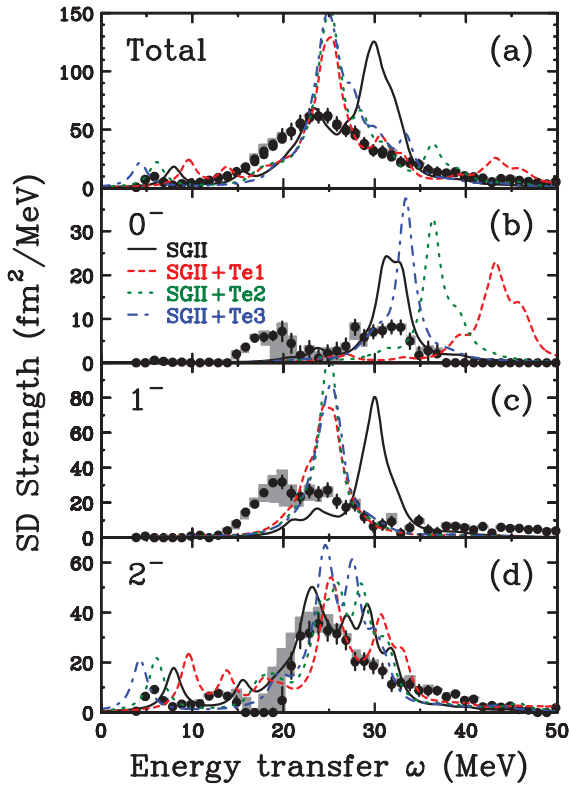$$

FIG. 19. (Color online) As described for Fig. 18, but including the HF + RPA predictions [22] for comparison with the data. The solid, dashed, dotted, and dot-dashed curves represent the results with the SGII, SGII + Te1, SGII + Te2, and SGII + Te3 interactions, respectively. The discrete RPA results have been smoothed by Lorentzian averaging with a width of 1 MeV. See text for details.
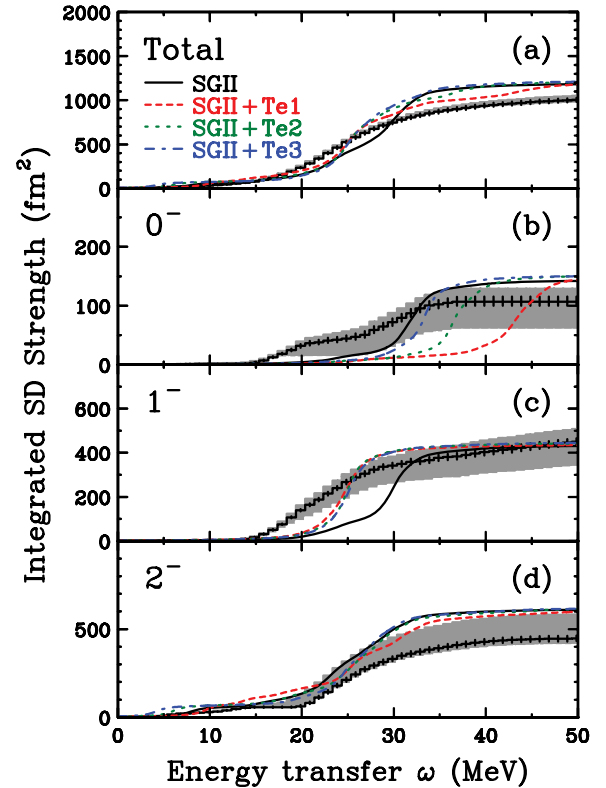

FIG. 20. (Color online) The integrated SD strengths defined in Eq. (27). The separated SD strengths are presented in panels (b)–(d) for $\Delta J^\pi = 0^-$, 1^-, and 2^-, respectively, and the total SD strength is shown in panel (a). The bands represent the uncertainties arising from the selection of α in Eq. (18). The solid, dashed, dotted, and dot-dashed curves represent the HF + RPA predictions [22] with the SGII, SGII + Te1, SGII + Te2, and SGII + Te3 interactions, respectively.

The solid, dashed, dotted, and dot-dashed curves represent the HF + RPA results with the SGII, SGII + Te1, SGII + Te2, and SGII + Te3 interactions, respectively. The SGII + Te3 results give qualitative descriptions for both the separated and total SD strengths. However, the theoretical predictions overestimate the total strengths by approximately 30% for $\Delta J^\pi = 0^-$ and 2^-. The present SD strengths have fairly large uncertainties arising from the selection of α in Eq. (18), which is indicated by the bands in Fig. 20. Furthermore, other sources of uncertainty exist for which no assessment is currently available, such as possible quenching of the SD strengths or interference between SD and other excitations with the same ΔJ^π. Therefore, further detailed theoretical investigations are required to assess the effects of quenching on the SD strengths.

VII. SUMMARY AND CONCLUSION

Measurements of the cross sections and analyzing powers at $\theta_{\rm lab} = 0°–10°$ and complete sets of polarization transfer observables and induced polarizations at $\theta_{\rm lab} = 0°–7°$ were performed for the $^{208}{\rm Pb}(p, n)$ reaction at $T_p = 296$ MeV. The experimental data were compared with those obtained using DWIA calculations employing RPA response functions. The GT giant resonance at $\theta_{\rm lab} \lesssim 2°$ was reasonably reproduced by the DWIA + RPA calculations with appropriate normalization. In contrast, the SD resonance and other excitations at $\theta_{\rm lab} \gtrsim 4.0°$ were not reproduced particularly well. Furthermore, the calculations underestimate the cross sections at $\omega \gtrsim 35$ MeV, which is due to neglecting the effect of configuration mixing, such as the coupling to $2p$-$2h$ excitations beyond the RPA.

MD analysis was performed to deduce the GT and SD strengths in the continuum. In the analysis, the polarization observables were included, for the first time, to separate the SD strengths into individual multipole contributions. There is significant $\Delta J^\pi = 1^+$ strength in the continuum beyond the GT giant resonance, which is due to both the configuration mixing and IVSM contributions. To determine each GT and IVSM strength, detailed information on the interference effects that occur between the GT and IVSM transitions is required.

The SD strengths were successfully separated into individual ΔJ^π components. A ΔJ^π dependence is clearly evident in the SD strength distributions and is reasonably reproduced by HF + RPA calculations including the Skyrme interaction with tensor components. The present findings, and further applications of polarization transfer measurements to other nuclei, will provide valuable insight into nuclear structure, such as tensor interaction effects in nuclear spin excitations.

[1] M. N. Harakeh and A. van der Woude, *Giant Resonances: Fundamental High-Frequency Modes of Nuclear Excitation* (Oxford University Press, Oxford, 2001).

[2] C. Gaarde, Nucl. Phys. A **396**, 127c (1983).

[3] C. Gaarde *et al.*, Nucl. Phys. A **369**, 258 (1981).

[4] K. Ikeda, S. Fujita, and J. I. Fujita, Phys. Lett. **3**, 271 (1963).

[5] K. Shimizu, M. Ichimura, and A. Arima, Nucl. Phys. A **226**, 282 (1974).

[6] G. F. Bertsch and I. Hamamoto, Phys. Rev. C **26**, 1323 (1982).

[7] M. Ericson, A. Figureau, and C. Thévenet, Phys. Lett. B **45**, 19 (1973).

[8] E. Oset and M. Rho, Phys. Rev. Lett. **42**, 47 (1979).

[9] H. Toki and W. Weise, Phys. Lett. B **97**, 12 (1980).

[10] A. Bohr and B. R. Mottelson, Phys. Lett. B **100**, 10 (1981).

[11] T. Wakasa *et al.*, Phys. Rev. C **55**, 2909 (1997).

[12] K. Yako *et al.*, Phys. Lett. B **615**, 193 (2005).

[13] M. Ichimura, H. Sakai, and T. Wakasa, Prog. Part. Nucl. Phys. **56**, 446 (2006).

[14] C. L. Bai, H. Q. Zhang, X. Z. Zhang, F. R. Xu, H. Sagawa, and G. Colò, Phys. Rev. C **79**, 041301(R) (2009).

[15] W. P. Alford and B. M. Spicer, Adv. Nucl. Phys. **24**, 1 (1994).

[16] K. Yako, H. Sagawa, and H. Sakai, Phys. Rev. C **74**, 051303(R) (2006).

[17] V. F. Dmitriev, V. Zelevinsky, and S. M. Austin, Phys. Rev. C **65**, 015803 (2001).

[18] S. Drożdż, F. Osterfeld, J. Speth, and J. Wambach, Phys. Lett. B **189**, 271 (1987).

[19] T. Suzuki and H. Sagawa, Nucl. Phys. A **637**, 547 (1998).

[20] T. Suzuki, Nucl. Phys. A **687**, 119c (2001).

[21] C. L. Bai, H. Q. Zhang, H. Sagawa, X. Z. Zhang, G. Colò, and F. R. Xu, Phys. Rev. Lett. **105**, 072501 (2010).

[22] C. L. Bai, H. Q. Zhang, H. Sagawa, X. Z. Zhang, G. Colò, and F. R. Xu, Phys. Rev. C **83**, 054316 (2011).

[23] H. Sagawa *et al.*, Phys. Rev. C **76**, 024301 (2007).

[24] H. Sakai *et al.*, Nucl. Instrum. Methods Phys. Res. A **369**, 120 (1996).

[25] T. Wakasa *et al.*, RCNP Annual Report, 1994, p. 14.

[26] T. Wakasa *et al.*, Nucl. Instrum. Methods Phys. Res. A **404**, 355 (1998).

[27] T. Wakasa *et al.*, Nucl. Instrum. Methods Phys. Res. A **547**, 569 (2005).

[28] T. Wakasa *et al.*, J. Phys. Soc. Jpn. **73**, 1611 (2004).

[29] K. Hatanaka *et al.*, Nucl. Instrum. Methods Phys. Res. A **384**, 575 (1997).

[30] T. Wakasa *et al.*, Phys. Rev. C **59**, 3177 (1999).

[31] T. N. Taddeucci *et al.*, Phys. Rev. C **41**, 2548 (1990).

[32] M. W. McNaughton *et al.*, Phys. Rev. C **45**, 2564 (1992).

[33] M. Dozono *et al.*, J. Phys. Soc. Jpn. **77**, 014201 (2008).

[34] J. M. Moss, Phys. Rev. C **26**, 727 (1982).

[35] T. Wakasa, M. Okamoto, M. Takaki, M. Dozono, K. Hatanaka, M. Ichimura, T. Noro, H. Okamura, and Y. Sakemi, Phys. Rev. C **84**, 014614 (2011).

[36] K. Kawahigashi *et al.*, Phys. Rev. C **63**, 044609 (2001).

[37] K. Nishida and M. Ichimura, Phys. Rev. C **51**, 269 (1995).

[38] R. Machleidt, K. Holinde, and C. Elster, Phys. Rep. **149**, 1 (1987).

[39] T. Wakasa, M. Ichimura, and H. Sakai, Phys. Rev. C **72**, 067303 (2005).

[40] T. Suzuki, Phys. Lett. B **104**, 92 (1981).

[41] G. Bertsch, D. Cha, and H. Toki, Phys. Rev. C **24**, 533 (1981).

[42] W. H. Dickhoff *et al.*, Phys. Rev. C **23**, 1154 (1981).

[43] M. J. Martin, Nucl. Data Sheets **108**, 1583 (2007).

[44] P. Ring and J. Speth, Phys. Lett. B **44**, 477 (1973).

[45] F. Osterfeld, Rev. Mod. Phys. **64**, 491 (1992).

[46] A. Bohr and B. R. Mottelson, *Nuclear Structure Volume I: Single-Particle Motion* (Benjamin, New York, 1969).

[47] N. V. Giai and P. V. Thieu, Phys. Lett. B **126**, 421 (1983).

[48] C. Mahaux and R. Sartor, Nucl. Phys. A **481**, 381 (1988).

[49] R. D. Smith and J. Wambach, Phys. Rev. C **38**, 100 (1988).

[50] S. Fantoni and V. R. Pandharipande, Nucl. Phys. A **473**, 234 (1987).

[51] M. A. Franey and W. G. Love, Phys. Rev. C **31**, 488 (1985).

[52] E. D. Cooper *et al.*, Phys. Rev. C **47**, 297 (1993).

[53] S. Qing-biao, F. Da-chun, and Z. Yi-zhong, Phys. Rev. C **43**, 2773 (1991).

[54] E. Bleszynski, M. Bleszynski, and J. C. A. Whitten, Phys. Rev. C **26**, 2063 (1982).

[55] M. Ichimura and K. Kawahigashi, Phys. Rev. C **45**, 1822 (1992).

[56] K. Yako *et al.*, Phys. Rev. Lett. **103**, 012503 (2009).

[57] K. Yako, Ph.D. thesis, University of Tokyo, 2002.

[58] T. N. Taddeucci *et al.*, Nucl. Phys. A **469**, 125 (1987).

[59] M. Sasano *et al.*, Phys. Rev. C **79**, 024602 (2009).

[60] N. Auerbach and A. Klein, Phys. Rev. C **30**, 1032 (1984).

[61] I. Hamamoto and H. Sagawa, Phys. Rev. C **62**, 024319 (2000).

[62] N. D. Dang, A. Arima, T. Suzuki, and S. Yamaji, Phys. Rev. Lett. **79**, 1638 (1997).

[63] D. L. Prout *et al.*, Phys. Rev. C **63**, 014603 (2000).

[64] R. G. T. Zegers *et al.*, Phys. Rev. Lett. **90**, 202501 (2003).

[65] R. G. T. Zegers *et al.*, Phys. Rev. C **63**, 034613 (2001).

[66] M. A. Hofstee *et al.*, Nucl. Phys. A **588**, 729 (1995).

[67] N. Auerbach, Comments Nucl. Part. Phys. **32**, 223 (1998).

[68] K. Yako, H. Sagawa, and H. Sakai, Phys. Rev. C **74**, 051303(R) (2006).

[69] T. H. R. Skyrme, Nucl. Phys. **9**, 615 (1959).

[70] M. Bender, P.-H. Heenen, and P.-G. Reinhard, Rev. Mod. Phys. **75**, 121 (2003).

[71] G. Colò, AIP Conf. Proc. **1128**, 59 (2009).

[72] B. A. Brown, T. Duguet, T. Otsuka, D. Abe, and T. Suzuki, Phys. Rev. C **74**, 061303(R) (2006).

[73] J. Dobaczewski, in *Proceedings of the Third ANL/MSU/JINA/INT RIA Workshop*, edited by T. Duguet, H. Esbensen, K. M. Nollett and C. D. Roberts (World Scientific, Singapore, 2006).

[74] G. Colò, H. Sagawa, S. Fracasso, and P. F. Bortignon, Phys. Lett. B **646**, 227 (2007).

[75] D. M. Brink and F. Stancu, Phys. Rev. C **75**, 064311 (2007).

[76] T. Lesinski, M. Bender, K. Bennaceur, T. Duguet, and J. Meyer, Phys. Rev. C **76**, 014312 (2007).

[77] M. Grasso, Z. Y. Ma, E. Khan, J. Margueron, and N. V. Giai, Phys. Rev. C **76**, 044319 (2007).

[78] W. Zou, G. Colò, Z. Ma, H. Sagawa, and P. F. Bortignon, Phys. Rev. C **77**, 014314 (2008).

[79] M. Zalewski, J. Dobaczewski, W. Satuła, and T. R. Werner, Phys. Rev. C **77**, 024316 (2008).

[80] T. Otsuka, T. Suzuki, R. Fujimoto, H. Grawe, and Y. Akaishi, Phys. Rev. Lett. **95**, 232502 (2005).

[81] T. Otsuka, T. Matsuo, and D. Abe, Phys. Rev. Lett. **97**, 162501 (2006).

[82] C. L. Bai, H. Sagawa, H. Q. Zhang, X. Z. Zhang, G. Colò, and F. R. Xu, Phys. Lett. B **675**, 28 (2009).

[83] L. Cao, G. Colò, H. Sagawa, P. F. Bortignon, and L. Sciacchitano, Phys. Rev. C **80**, 064304 (2009).

[84] F. Stancu, D. M. Brink, and H. Flocard, Phys. Lett. B **68**, 108 (1977).